



This is a repository copy of *Managing phase purities and crystal orientation for high-performance and photostable cesium lead halide perovskite solar cells.*

White Rose Research Online URL for this paper:  
<https://eprints.whiterose.ac.uk/161637/>

Version: Published Version

---

**Article:**

Wang, Q., Smith, J.A. [orcid.org/0000-0001-6889-4408](https://orcid.org/0000-0001-6889-4408), Skroblin, D. et al. (10 more authors) (2020) Managing phase purities and crystal orientation for high-performance and photostable cesium lead halide perovskite solar cells. *Solar RRL*, 4 (9). 2000213. ISSN 2367-198X

<https://doi.org/10.1002/solr.202000213>

---

**Reuse**

This article is distributed under the terms of the Creative Commons Attribution (CC BY) licence. This licence allows you to distribute, remix, tweak, and build upon the work, even commercially, as long as you credit the authors for the original work. More information and the full terms of the licence here:  
<https://creativecommons.org/licenses/>

**Takedown**

If you consider content in White Rose Research Online to be in breach of UK law, please notify us by emailing [eprints@whiterose.ac.uk](mailto:eprints@whiterose.ac.uk) including the URL of the record and the reason for the withdrawal request.



[eprints@whiterose.ac.uk](mailto:eprints@whiterose.ac.uk)  
<https://eprints.whiterose.ac.uk/>

# Managing Phase Purities and Crystal Orientation for High-Performance and Photostable Cesium Lead Halide Perovskite Solar Cells

Qiong Wang,\* Joel A. Smith, Dieter Skroblin, Julian A. Steele, Christian M. Wolff, Pietro Caprioglio, Martin Stolterfoht, Hans Köbler, Meng Li, Silver-Hamill Turren-Cruz, Christian Gollwitzer, Dieter Neher, and Antonio Abate\*

Inorganic perovskites with cesium ( $\text{Cs}^+$ ) as the cation have great potential as photovoltaic materials if their phase purity and stability can be addressed. Herein, a series of inorganic perovskites is studied, and it is found that the power conversion efficiency of solar cells with compositions  $\text{CsPbI}_{1.8}\text{Br}_{1.2}$ ,  $\text{CsPbI}_{2.0}\text{Br}_{1.0}$ , and  $\text{CsPbI}_{2.2}\text{Br}_{0.8}$  exhibits a high dependence on the initial annealing step that is found to significantly affect the crystallization and texture behavior of the final perovskite film. At its optimized annealing temperature,  $\text{CsPbI}_{1.8}\text{Br}_{1.2}$  exhibits a pure orthorhombic phase and only one crystal orientation of the (110) plane. Consequently, this allows for the best efficiency of up to 14.6% and the longest operational lifetime,  $T_{\text{S80}}$ , of  $\approx 300$  h, averaged of over six solar cells, during the maximum power point tracking measurement under continuous light illumination and nitrogen atmosphere. This work provides essential progress on the enhancement of photovoltaic performance and stability of  $\text{CsPbI}_{3-x}\text{Br}_x$  perovskite solar cells.

## 1. Introduction


Inorganic cesium lead halide perovskites, expressed in brief as  $\text{CsPbI}_{3-x}\text{Br}_x$  with  $x$  ranging from 0 to 3, have been under intense investigation for photovoltaic applications.<sup>[1–3]</sup> In contrast to lead halide perovskites containing volatile organic cations, such as methyl ammonium,<sup>[4]</sup> cesium lead halides exhibit excellent thermal stability. Although pure iodide  $\text{CsPbI}_3$  has the most promising bandgap of  $\approx 1.7$  eV, the inherent thermodynamic instability of its photoactive cubic ( $\alpha$ ) phase at room temperature remains challenging.<sup>[5]</sup> Recent works on  $\text{CsPbI}_3$  have used a promising strategy to make a relatively low bandgap (1.68 eV) inorganic perovskite with high efficiencies.<sup>[2,6,7]</sup>

Dr. Q. Wang, H. Köbler, Dr. M. Li, Dr. S.-H. Turren-Cruz, Prof. A. Abate  
 Young Investigator Group Active Materials and Interfaces for Stable Perovskite Solar Cells  
 Helmholtz-Zentrum Berlin für Materialien und Energie  
 Kekuléstraße 5, Berlin 12489, Germany  
 E-mail: qiong.wang@helmholtz-berlin.de;  
 antonio.abate@helmholtz-berlin.de

J. A. Smith  
 Department of Physics and Astronomy  
 University of Sheffield  
 Hicks Building, Hounsfield Road, Sheffield S3 7RH, UK

D. Skroblin, Prof. C. Gollwitzer  
 Physikalisch-Technische Bundesanstalt (PTB)  
 Abbestraße 2-12, Berlin 10587, Germany

Dr. J. A. Steele  
 cMACS  
 Department of Microbial and Molecular Systems  
 KU Leuven  
 Celestijnenlaan 200F, Leuven 3001, Belgium

 The ORCID identification number(s) for the author(s) of this article can be found under <https://doi.org/10.1002/solr.202000213>.

© 2020 The Authors. Published by WILEY-VCH Verlag GmbH & Co. KGaA, Weinheim. This is an open access article under the terms of the Creative Commons Attribution License, which permits use, distribution and reproduction in any medium, provided the original work is properly cited.

DOI: 10.1002/solr.202000213

C. M. Wolff, P. Caprioglio, Dr. M. Stolterfoht, Prof. D. Neher  
 Institute for Physics and Astronomy  
 University of Potsdam  
 Karl-Liebknecht-Straße 24–25, Potsdam, Golm 14476, Germany

P. Caprioglio  
 Young Investigator Group Perovskite Tandem Solar Cells  
 Helmholtz-Zentrum Berlin für Materialien und Energie GmbH  
 Kekuléstraße 5, Berlin 12489, Germany

Dr. M. Li  
 Jiangsu Key Laboratory for Carbon-Based Functional Materials & Devices  
 Institute of Functional Nano & Soft Materials (FUNSOM)  
 Soochow University  
 Suzhou 215123, China

Prof. A. Abate  
 Department of Chemical, Materials and Production Engineering  
 University of Naples Federico II  
 Piazzale Tecchio 80, Naples, Fuorigrotta 80125, Italy

Prof. A. Abate  
 State Key Laboratory of Photocatalysis on Energy and Environment  
 Institute of Advanced Energy Materials  
 Fuzhou University  
 Fuzhou, Fujian 350002, China

By integrating the organic cation dimethylammonium ( $\text{DMA}^+$ ) into the precursor solution of  $\text{CsPbI}_3$  perovskite, crystallization of the tetragonal ( $\beta$ ) phase of  $\text{CsPbI}_3$  perovskite can be improved, and the phase better stabilized.<sup>[2,6]</sup>  $\text{DMA}^+$  in  $\text{CsPbI}_3$  would beneficially increase the Goldschmidt tolerance factor, however, whether it remains in the resultant film is still debated<sup>[2,8]</sup> and is likely annealing temperature-dependent.<sup>[8]</sup> An alternative strategy to achieve stability is through halide alloying with bromide in  $\text{CsPbI}_{3-x}\text{Br}_x$  compositions, which has the further advantage of optical bandgap tenability across a range of phase-stable perovskite compositions (in an inert atmosphere at room temperature).<sup>[9,10]</sup> Indeed, many works on  $\text{CsPbI}_2\text{Br}$  perovskite have shown significant progress with the photovoltaic performance.<sup>[9,11,12]</sup>

In our previous work,<sup>[13]</sup> we studied stable compositions of  $\text{CsPbI}_{3-x}\text{Br}_x$  prepared using pulsed flash infrared annealing. We found that with a bromide ratio ( $x$ ) of no less than 1.2, the compounds showed negligible degradation under environmental conditions (relative humidity of 30% at 25 °C) in either absorption or X-ray diffraction (XRD) measurements. As such, we investigated perovskite solar cells with  $x = 1.2, 1.5,$  and  $1.8$ ; however, these halide compositions have an optical bandgap of over 1.93 eV, which significantly limits their light-harvesting capability and results in devices with low photocurrent and power conversion efficiency (PCE). For a two-junction tandem cell, with a crystalline silicon<sup>[14]</sup> or  $\text{Cu(In, Ga)Se}_2$ <sup>[3]</sup> thin film that has a bandgap no wider than 1.2 eV as the bottom cell, a top cell with a bandgap in the range of 1.7–1.8 eV is required to provide an optimal short-circuit photocurrent density ( $J_{sc}$ ) of over  $18 \text{ mA cm}^{-2}$ , to match that of the bottom cell. For all-perovskite tandem cells, the wide-bandgap layer could be up to 1.9 eV, because the narrow bandgap perovskite with metal alloying of lead and tin has a minimum bandgap beyond 1.2 eV.<sup>[15]</sup> Recent works on all-perovskite tandem cells used tin-lead mixed perovskite with a narrow bandgap of 1.22,<sup>[16]</sup> 1.25,<sup>[17]</sup> and 1.27 eV<sup>[18]</sup> and the wide bandgap perovskite of 1.77, 1.75, and 1.8 eV correspondingly. Meanwhile, the photocurrent required from the wide bandgap perovskite in all-perovskite tandem cells can be as low as  $16 \text{ mA cm}^{-2}$ , opening the possibility for  $\text{CsPbI}_{3-x}\text{Br}_x$  with  $x$  up to a value of 1.2.

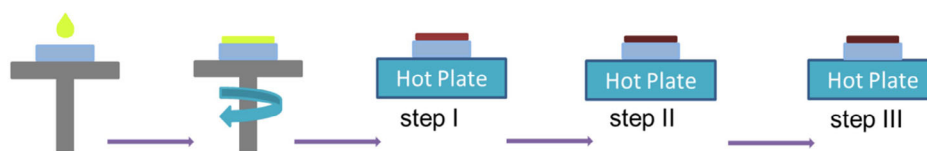
In this work, we studied the photostability [light soaking under maximum power point (MPP) tracking] of solar cells composed of  $\text{CsPbI}_{3-x}\text{Br}_x$  with low bromide content in a nitrogen atmosphere, to exclude the influence of moisture on the crystal structure of  $\text{CsPbI}_{3-x}\text{Br}_x$ . More specifically, we reduced the bromide content in  $\text{CsPbI}_{3-x}\text{Br}_x$  with  $x$  from 1.2 to 0.3 and studied the influence of the bromide content on the optical properties and crystallization behavior. We found that the first annealing step in a three-step annealing process played a critical role in determining the final film texture and phase behavior. In devices, this translated into significant solar cells performance

variation for the compositions  $\text{CsPbI}_{1.8}\text{Br}_{1.2}$ ,  $\text{CsPbI}_{2.0}\text{Br}_{1.0}$ , and  $\text{CsPbI}_{2.2}\text{Br}_{0.8}$ , depending on the temperature of the first step. Phase impurity, with photoinactive regions of a  $\delta$ -phase in  $\text{CsPbI}_{2.0}\text{Br}_{1.0}$  and  $\text{CsPbI}_{2.2}\text{Br}_{0.8}$  films, resulted in less ideal quantum efficiency for  $\text{CsPbI}_{2.0}\text{Br}_{1.0}$  (less than 90%) and  $\text{CsPbI}_{2.2}\text{Br}_{0.8}$  (less than 85%) perovskite solar cells. In the case of  $\text{CsPbI}_{1.8}\text{Br}_{1.2}$ , we found a low first annealing step temperature (42 °C) resulted in non-perovskite phase impurity, whereas a high first annealing step temperature (60 °C) led to more than one crystallographic orientation of the perovskite phase. At the optimized annealing temperature of 50 °C,  $\text{CsPbI}_{1.8}\text{Br}_{1.2}$  films showed the highest phase purity of the photoactive orthorhombic perovskite phase and only one dominant crystal orientation, with (110) oriented in the out-of-plane (OOP) direction. This scenario resulted in the highest PCE of up to 14.6% with external quantum efficiencies (EQEs) of over 90% in a broad spectral range of 450–560 nm. Moreover, these devices exhibited excellent solar cell performance and photostability over 300 h of MPP tracking, under continuous light illumination in a nitrogen atmosphere. This work provides further insights into the enhancement of operational lifetime of perovskite solar cells.

## 2. Results and Discussion

**Scheme 1** shows the deposition protocol we used for  $\text{CsPbI}_{3-x}\text{Br}_x$  thin films; further details of this process are described in the Experimental Section (see Supporting Information). In brief, we used an antisolvent-free crystallization approach; after spin coating, the substrates were processed with three annealing steps at three temperatures. For  $\text{CsPbI}_{1.8}\text{Br}_{1.2}$ ,  $\text{CsPbI}_{2.0}\text{Br}_{1.0}$ , and  $\text{CsPbI}_{2.2}\text{Br}_{0.8}$  perovskite films, the annealing temperatures for step II and step III were set at 100 and 160 °C, whereas we studied the influence of the temperature in step I on the final product. For  $\text{CsPbI}_{2.4}\text{Br}_{0.6}$  and  $\text{CsPbI}_{2.7}\text{Br}_{0.3}$  perovskite films, the annealing temperatures for step II and step III were set at 150 and 310 °C to form a black phase. It should be noted that  $\text{CsPbI}_{1.8}\text{Br}_{1.2}$ ,  $\text{CsPbI}_{2.0}\text{Br}_{1.0}$ , and  $\text{CsPbI}_{2.2}\text{Br}_{0.8}$  perovskite films all became darker after annealing in step II and step III compared with step I. In contrast,  $\text{CsPbI}_{2.4}\text{Br}_{0.6}$  and  $\text{CsPbI}_{2.7}\text{Br}_{0.3}$  perovskite films first formed a brown film in step I, and then transitioned first through a colorless phase in step II, and finally, a dark brown film formed in step III.

We first investigated the optical and structural properties across a broad mixed-halide compositional range. **Figure 1a** shows the recorded  $T_{auc}$  plots for the various  $\text{CsPbI}_{3-x}\text{Br}_x$  perovskites prepared using the method given in **Scheme 1**. The absorption coefficient ( $\alpha$ ) of  $\text{CsPbI}_{3-x}\text{Br}_x$  perovskite given in **Figure S1a**, Supporting Information, is comparable to that of organic cation-containing lead halide perovskite, such as methylammonium lead iodide ( $\text{MAPbI}_3$ ),<sup>[20]</sup> with all films



**Scheme 1.** Illustration of the deposition process of  $\text{CsPbI}_{3-x}\text{Br}_x$  thin films using a three-annealing step process adapted from the literature.<sup>[19]</sup>

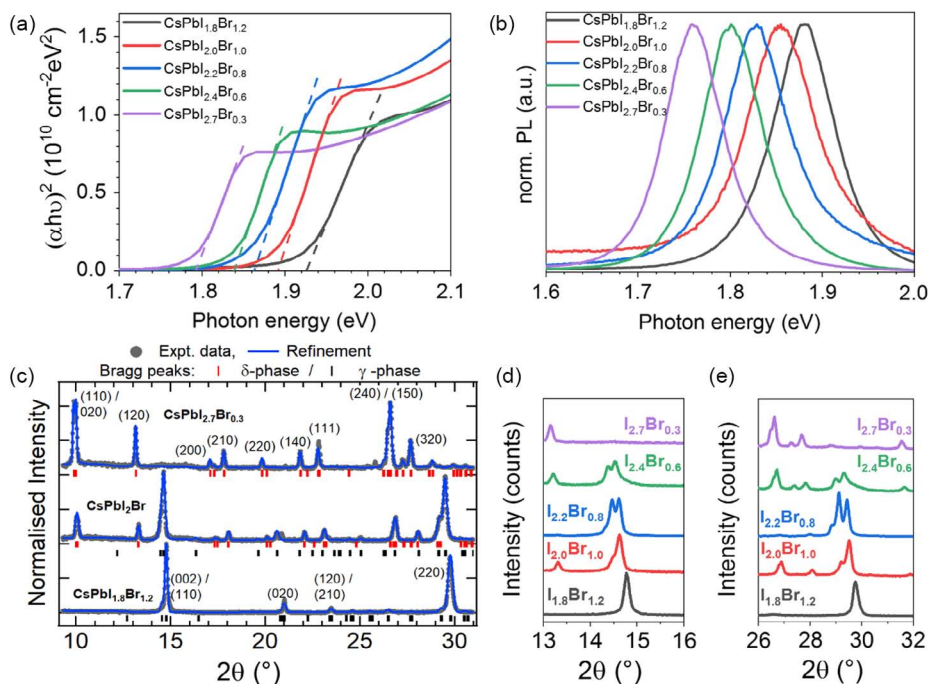


**Figure 1.** a) Tauc plots and b) steady-state PL spectra for the CsPbI<sub>3-x</sub>Br<sub>x</sub> perovskite compositional series. c) Thin-film XRD and structural refinement results for CsPbI<sub>1.8</sub>Br<sub>1.2</sub>, CsPbI<sub>2.0</sub>Br<sub>1.0</sub>, and CsPbI<sub>2.7</sub>Br<sub>0.3</sub>. d,e) Enlargements of XRD patterns for all compositions, highlighting the first-order perovskite reflections at d) 2θ of ≈14.5° and e) the second order of ≈29°. Samples for the UV–Vis spectra and XRD measurement were prepared using the stack of fluorine-doped tin oxide (FTO)/c-TiO<sub>2</sub>/m-TiO<sub>2</sub>/perovskite. Samples for PL spectra were prepared directly on insulating substrates.

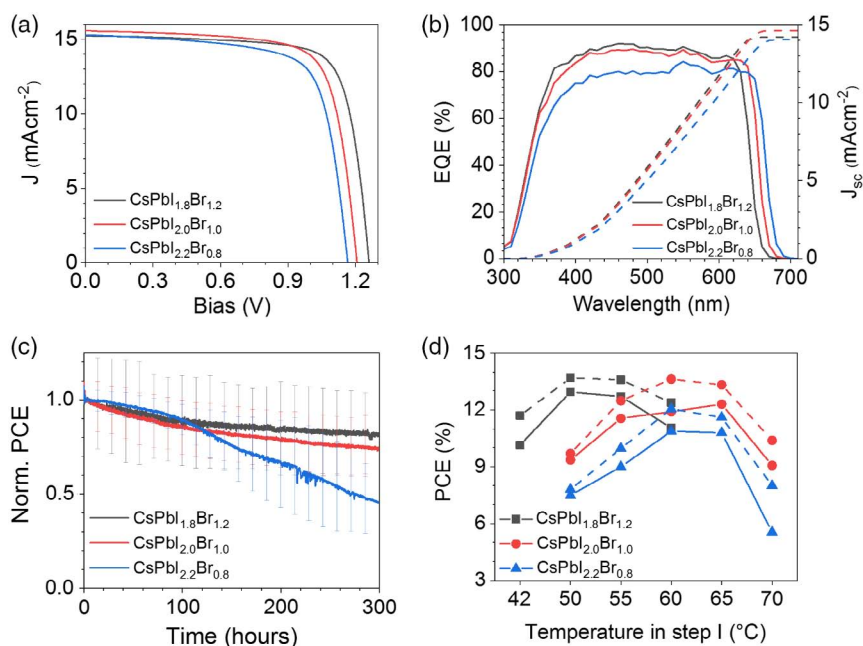
exhibiting a sharp absorption onset. This indicates that the photoactive CsPbI<sub>3-x</sub>Br<sub>x</sub> perovskite phases have strong light absorption, comparable to their hybrid organic counterparts. Figure 1b shows the steady-state photoluminescence (PL) spectra of cesium lead halides neat films, with emission peaks at photon energies of 1.88, 1.86, 1.83, 1.80, and 1.76 eV for CsPbI<sub>1.8</sub>Br<sub>1.2</sub>, CsPbI<sub>2.0</sub>Br<sub>1.0</sub>, CsPbI<sub>2.2</sub>Br<sub>0.8</sub>, CsPbI<sub>2.4</sub>Br<sub>0.6</sub>, and CsPbI<sub>2.7</sub>Br<sub>0.3</sub>, respectively. The optical bandgaps calculated from Tauc plots are 1.93, 1.89, 1.86, 1.84, and 1.79 eV for corresponding films. This confirms that the Stokes shift between the absorption, and emission for hybrid organic cation-containing perovskites<sup>[21]</sup> is also observed in inorganic perovskites.<sup>[22]</sup> Figure S2, Supporting Information, presents the linear dependence of the optical bandgap ( $E_g$ ) as a function of bromide content in CsPbI<sub>3-x</sub>Br<sub>x</sub> perovskites fabricated via the above-mentioned method, which can be expressed as  $E_g = 1.71 \text{ eV} + 0.21 * x$ .

Figure 1c shows the XRD patterns with structural refinement results (Le Bail method) for CsPbI<sub>1.8</sub>Br<sub>1.2</sub>, CsPbI<sub>2.0</sub>Br<sub>1.0</sub>, and CsPbI<sub>2.7</sub>Br<sub>0.3</sub> films. The results for CsPbI<sub>2.2</sub>Br<sub>0.8</sub> and CsPbI<sub>2.4</sub>Br<sub>0.6</sub> are given in Figure S3, Supporting Information. Although there are literature reports of cubic ( $\alpha$ ) phase CsPbI<sub>2.0</sub>Br<sub>1.0</sub> perovskites,<sup>[9,12,19]</sup> here, we show that in the range of compositions investigated via this processing route, the primary perovskite phase appears to be a distorted orthorhombic ( $\gamma$ -phase) at room temperature.<sup>[13,23]</sup> More importantly, CsPbI<sub>1.8</sub>Br<sub>1.2</sub> exhibits a pure  $\gamma$ -phase, and in the more I-rich perovskites, there is a mixture of a  $\gamma$ -phase and a non-perovskite  $\delta$ -phase, whereas CsPbI<sub>2.7</sub>Br<sub>0.3</sub> exhibits a pure  $\delta$ -phase. The enlarged XRD patterns in Figure 1d,e at 2θ of ≈14.5° and

≈29° highlight a shift to lower angles for the (110)/(002) and (220)/(004) scattering as the bromide content decreases, indicating a larger unit cell with more I-rich perovskite compositions. Moreover, (110)/(002) and (220)/(004) peaks splitting becomes more pronounced as the bromide content is reduced from  $x = 1.2$  to 0.8.

Next, we prepared solar cells across the CsPbI<sub>3-x</sub>Br<sub>x</sub> perovskite compositional series, as described in the Experimental Section (see Supporting Information). Figure S4, Supporting Information, presents the  $J$ - $V$  curves for the best CsPbI<sub>2.4</sub>Br<sub>0.6</sub> and CsPbI<sub>2.7</sub>Br<sub>0.3</sub> solar cells with a PCE of 5.12% and 9.45%. Table S1, Supporting Information, summarizes the photovoltaic parameters. Unfortunately, these devices quickly degraded after 1 day to less than half of their initial PCEs despite storage inside a nitrogen-filled glovebox. We think the poor stability in these I-rich devices could be caused by the less phase stability of I-rich perovskites. As such, for these compositions, alternative strategies must be developed to enhance phase formation and stability, which we will continue to investigate.

Figure 2a gives the  $J$ - $V$  curves of the champion devices for CsPbI<sub>1.8</sub>Br<sub>1.2</sub>, CsPbI<sub>2.0</sub>Br<sub>1.0</sub>, and CsPbI<sub>2.2</sub>Br<sub>0.8</sub> with PCEs of 14.6%, 13.9%, and 12.8%, respectively. With the decrease in bromide content and bandgap, the open-circuit voltage ( $V_{oc}$ ) is reduced from 1261 mV (CsPbI<sub>1.8</sub>Br<sub>1.2</sub>) to 1207 mV (CsPbI<sub>2.0</sub>Br<sub>1.0</sub>) to 1166 mV (CsPbI<sub>2.2</sub>Br<sub>0.8</sub>). Notably, with the CsPbI<sub>1.8</sub>Br<sub>1.2</sub> perovskite, we achieved among the highest reported  $V_{oc}$  values and PCEs for inorganic perovskite solar cells with a wide bandgap.<sup>[12,13,19,24]</sup> Although we might expect an increase in the photocurrent with more I-rich compounds, the value of



**Figure 2.** a)  $J$ - $V$  curves and b) EQE spectra of champion perovskite solar cells with compositions  $\text{CsPbI}_{1.8}\text{Br}_{1.2}$  (black line),  $\text{CsPbI}_{2.0}\text{Br}_{1.0}$  (red), and  $\text{CsPbI}_{2.2}\text{Br}_{0.8}$  (blue). c) MPP tracked performance for perovskite solar cells under constant 1 sun illumination and in a nitrogen atmosphere at room temperature, plotting normalized average efficiency of a minimum of six solar cells and the standard deviation as the error bar. d) Average (solid line) and champion (dashed line) efficiencies of perovskite solar cells for each composition dependent on the step I temperature.

$J_{sc}$  is quite similar for all compositions. This observation can be rationalized from EQE measurements given in Figure 2b. We find that for solar cells with composition  $\text{CsPbI}_{1.8}\text{Br}_{1.2}$ , the EQE peaks at  $\approx 90\%$  in the wavelength range from 450 to 560 nm and remain over 80% for most of the spectrum. The high EQE indicates efficient charge collection at short-circuit conditions for  $\text{CsPbI}_{1.8}\text{Br}_{1.2}$  perovskite solar cells. In contrast, the EQE of  $\text{CsPbI}_{2.0}\text{Br}_{1.0}$  perovskite solar cell peaks below 90%, and for the  $\text{CsPbI}_{2.2}\text{Br}_{0.8}$  device, the maximum EQE is  $\approx 80\%$ , indicating less effective charge extraction in these cells. The relatively low fill factor ( $FF$ ) in these solar cells also points to a charge extraction problem. As revealed in XRD measurements (Figure 1c and Figure S3, Supporting Information), the presence of photoinactive  $\delta$ -phase in  $\text{CsPbI}_{2.0}\text{Br}_{1.0}$  and  $\text{CsPbI}_{2.2}\text{Br}_{0.8}$  may impede charge extraction. Alternatively, the loss of  $J_{sc}$  in these devices could simply come from there being less absorbing material in the film. The series resistance ( $R_s$ ), estimated from the linear intercepts of the  $J$ - $V$  curves (Figure 2a) at  $J_{sc}$  and  $V_{oc}$  points, respectively, are summarized in Table S2, Supporting Information, together with the photovoltaic parameters of  $J$ - $V$  curve given in Figure 2a. We find a reduced  $R_s$  in the more I-rich devices, which could be explained by higher  $\delta$ -phase content and its interface with the perovskite phase contributing to more defects in the system. Interestingly,  $R_s$  was estimated to be lower in the more I-rich solar cells, revealing that the contact ohm resistance is decreased for perovskites with a smaller bandgap. Figure 2b also shows that  $\text{CsPbI}_{1.8}\text{Br}_{1.2}$ ,  $\text{CsPbI}_{2.0}\text{Br}_{1.0}$ , and  $\text{CsPbI}_{2.2}\text{Br}_{0.8}$  perovskite solar cells have the EQE spectral onset at 655, 666, and 677 nm, which agrees well with the absorption spectra given in Figure S1b, Supporting

Information. The integrated  $J_{sc}$  from EQE spectra shows a  $J_{sc}$  of 14.21, 14.62, and 14.05  $\text{mA cm}^{-2}$  for  $\text{CsPbI}_{1.8}\text{Br}_{1.2}$ ,  $\text{CsPbI}_{2.0}\text{Br}_{1.0}$ , and  $\text{CsPbI}_{2.2}\text{Br}_{0.8}$ , respectively. The value of  $J_{sc}$  extracted from  $J$ - $V$  measurement shows an overestimation of 7.0%, 6.7%, and 8.9% for  $\text{CsPbI}_{1.8}\text{Br}_{1.2}$ ,  $\text{CsPbI}_{2.0}\text{Br}_{1.0}$ , and  $\text{CsPbI}_{2.2}\text{Br}_{0.8}$ , respectively, compared with the EQE measurement. The absence of a shallow mask during the  $J$ - $V$  measurement may be the reason for an overestimation of the  $J_{sc}$ .<sup>[25]</sup>

We then investigated the photostability of devices with varying halide composition under operational conditions, with constant 1 sun illumination and MPP tracking. Figure 2c shows the normalized, averaged efficiency of at least six solar cells over 300 h of testing, conducted at room temperature and in a nitrogen atmosphere, adopting the ISOS-L-11 protocol.<sup>[26]</sup> The  $T_{S80}$  parameter, which represents the time taken for a solar cell to degrade to 80% of its maximum efficiency (counting from  $T_{max}$  when maximum efficiency is reached), is roughly 300 h for  $\text{CsPbI}_{1.8}\text{Br}_{1.2}$  perovskite solar cells, yet only around 192 h for  $\text{CsPbI}_{2.0}\text{Br}_{1.0}$  and 134 h for  $\text{CsPbI}_{2.2}\text{Br}_{0.8}$  perovskite solar cells. This demonstrates clearly that  $\text{CsPbI}_{1.8}\text{Br}_{1.2}$  cells have superior operational lifetime to  $\text{CsPbI}_{2.0}\text{Br}_{1.0}$  and  $\text{CsPbI}_{2.2}\text{Br}_{0.8}$  cells, with better performance retention during testing.

To further understand the perovskite phase formation process, we tried modifying the step I temperature and found that it plays a critical role in determining device efficiency. Figure 2d shows the efficiencies of solar cells fabricated when varying the annealing temperature in step I (as shown in Scheme 1). It shows that for all three compositions, both the average efficiency (solid line) and the champion efficiency (dashed line)

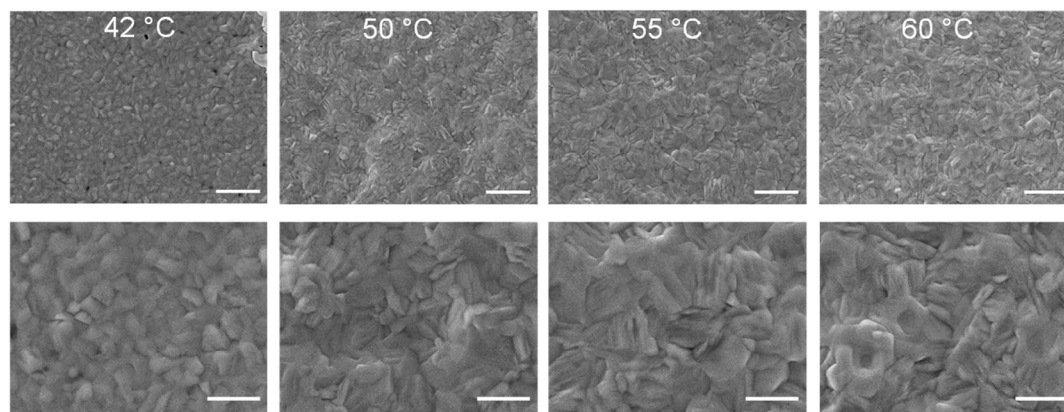
(dashed line) of cells have a similar performance trend, dependent on the temperature in step I. CsPbI<sub>1.8</sub>Br<sub>1.2</sub> perovskite solar cells are most efficient with the step I temperature of 50 °C. In contrast, CsPbI<sub>2.0</sub>Br<sub>1.0</sub> and CsPbI<sub>2.2</sub>Br<sub>0.8</sub> perovskite solar cells reach the highest efficiency at temperatures of 60 and 65 °C. This trend indicates that for this composition range, with higher bromide content, less thermal energy is required for the initial crystallization, consistent with lead bromide perovskite phases generally having lower formation enthalpies than iodide equivalent compounds.<sup>[27]</sup> We speculate that with this antisolvent-free processing route, step I removes remnant solvent and initiates the perovskite crystallization, which may proceed via an intermediate solvent-adduct phase, with the temperature and halide content both impacting the nucleation process.<sup>[19]</sup> As we will discuss in the following section, for the CsPbI<sub>1.8</sub>Br<sub>1.2</sub> perovskite, the selection of the temperature in step I has a significant influence on the final product. Box charts of photovoltaic parameters of solar cells prepared at different temperatures in step I are summarized in Figure S5, Supporting Information. An average efficiency of 12.94%, 11.90%, and 10.85% was achieved for CsPbI<sub>2.0</sub>Br<sub>1.0</sub>, CsPbI<sub>2.0</sub>Br<sub>1.0</sub>, and CsPbI<sub>2.2</sub>Br<sub>0.8</sub> perovskite solar cells at their optimal step I temperature.

CsPbI<sub>1.8</sub>Br<sub>1.2</sub> perovskite is studied as an example to understand the influence of the step I temperature on the optical and crystal structural properties of the films. First, we investigated the surface morphology using scanning electron microscopy (SEM). **Figure 3** shows the surface morphology of CsPbI<sub>1.8</sub>Br<sub>1.2</sub> samples prepared at four different step I temperatures, i.e., 42, 50, 55, and 60 °C. The low magnification SEM images in the top panels show that all of the perovskite films have good coverage on top of the mesoporous titanium dioxide (TiO<sub>2</sub>) layer. The high magnification SEM images along the bottom row show larger crystalline domains for CsPbI<sub>1.8</sub>Br<sub>1.2</sub> perovskite as the temperature in step I is increased from 42 to 60 °C. Between 42 and 50 °C, there is a significant evolution of morphology, and for 60 °C, the structure appears to be more merged or fused together. Cross-sectional SEM images of the films are given in Figure S6, Supporting Information, showing that all films have similar thicknesses of ≈500 nm. Organized, columnar grains are apparent for samples prepared at 50 °C, minimizing grain boundaries between

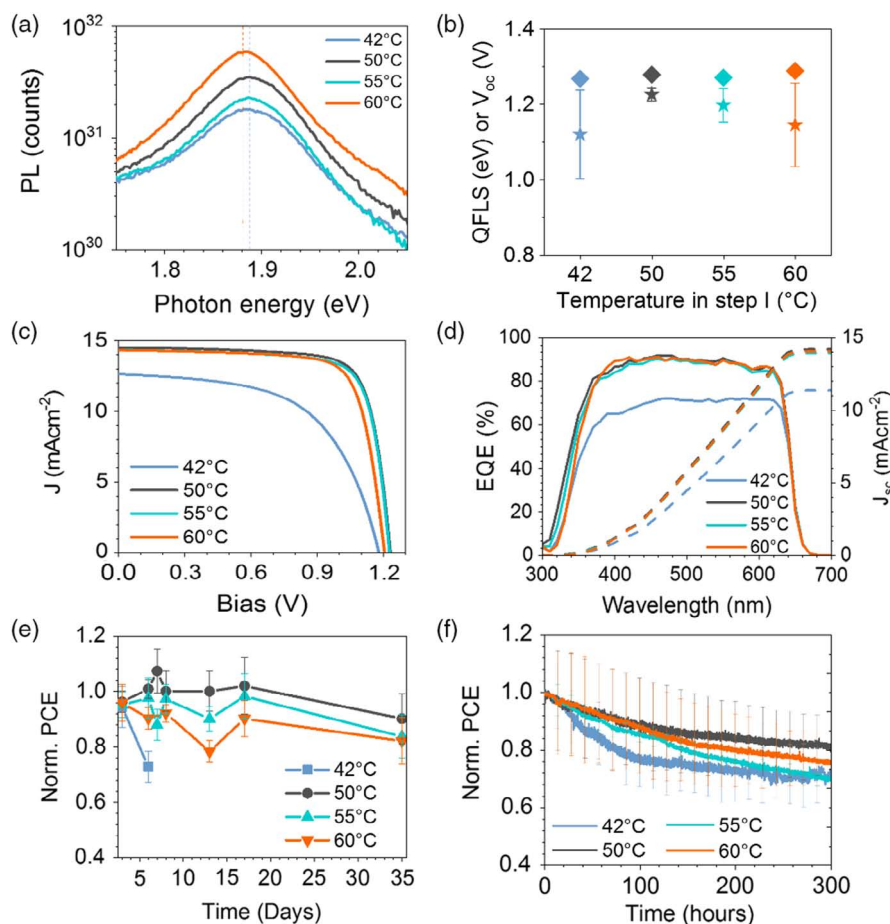
the selective contacts. This ideal grain growth is critical in enabling the highest efficiency of CsPbI<sub>1.8</sub>Br<sub>1.2</sub> cells, evident in an increase in *FF* from 52% to 75% when comparing 42 and 50 °C (Figure S5, Supporting Information).

Figure S7, Supporting Information, shows that the optical bandgap is negligibly influenced by the step I temperature. However, films prepared at 42 °C show a more gradual absorption onset and a slightly lower optical bandgap of 1.91 eV, compared with films made at other temperatures. As we will further discuss in the XRD and grazing-incidence wide-angle X-ray scattering (GIWAXS) measurements, this difference may originate from the presence of photoinactive domains ( $\delta$ -phase) in samples prepared at 42 °C. Despite this, **Figure 4a** reveals that the perovskite films in the stack of FTO/c-TiO<sub>2</sub>/m-TiO<sub>2</sub>/CsPbI<sub>1.8</sub>Br<sub>1.2</sub> have similar PL peak positions. Films prepared at 42 °C have the lowest PL intensity, followed by 55 and 50 °C, with 60 °C showing the highest PL intensity. Moreover, we calculated the internal quasi-Fermi level splitting (QFLS) from the absolute PL spectra following our previously reported approach.<sup>[28]</sup> The obtained QFLS is shown in **Figure 4b**, together with the *V*<sub>oc</sub> obtained from the *J*–*V* measurement. It shows that solar cells made at 50 °C have the highest *V*<sub>oc</sub> and the smallest potential loss (53 mV) when compared with the neat absorber on FTO/c-TiO<sub>2</sub>/m-TiO<sub>2</sub>. For CsPbI<sub>1.8</sub>Br<sub>1.2</sub> samples prepared with 60 °C step I temperature, we also notice the potential loss of up to 144 mV. As these samples show the highest QFLS, indicating reduced non-radiative recombination at the interface with TiO<sub>2</sub>, the high potential loss is very likely to originate from the interface with spiro-OMeTAD.<sup>[29]</sup> As we will discuss in the GIWAXS data, samples prepared at 60 °C resulted in two constrained crystal orientations or textures. In other words, the second facet orientation may cause an issue for the molecular interaction between CsPbI<sub>1.8</sub>Br<sub>1.2</sub> perovskite and spiro-OMeTAD.<sup>[30]</sup>

**Figure 4c** shows the *J*–*V* curves of champion perovskite solar cells prepared at each temperature. Solar cells made with the step I temperature of 50, 55, and 60 °C result in significantly enhanced *FF*, *V*<sub>oc</sub>, and *J*<sub>sc</sub>, compared with those prepared at 42 °C. The enhancement is also observed in the EQE spectra (**Figure 4d**). It presents that cells made at 42 °C may suffer from



**Figure 3.** SEM highlighting the surface morphology of CsPbI<sub>1.8</sub>Br<sub>1.2</sub> films as a function of the step I temperature. Layers were deposited on FTO/c-TiO<sub>2</sub>/m-TiO<sub>2</sub> to mimic completed devices. Scale bars are 2 μm for the top panels and 800 nm for the bottom panels.



**Figure 4.** a) Absolute PL spectra of CsPbI<sub>1.8</sub>Br<sub>1.2</sub> films, deposited on FTO/c-TiO<sub>2</sub>/m-TiO<sub>2</sub>. b) QFLS (diamonds, calculated from part a) and V<sub>oc</sub> (stars) from *J*–*V* measurements of CsPbI<sub>1.8</sub>Br<sub>1.2</sub> solar cells. c) *J*–*V* curve and d) EQE spectra of champion solar cells fabricated with composition CsPbI<sub>1.8</sub>Br<sub>1.2</sub>. e) Shelf-lifetime measurement of solar cells stored under nitrogen and in the dark, normalized to the initial mean efficiency, with *J*–*V* measurements conducted periodically and averaged from at least 12 solar cells. f) Operational lifetime testing of CsPbI<sub>1.8</sub>Br<sub>1.2</sub> solar cells, showing normalized average efficiency of a minimum of eight solar cells. MPP tracked performance, with constant 1 sun illumination in a nitrogen atmosphere and at room temperature. All error bars are calculated from the standard deviation.

poor charge collection with the EQE below 80% over the whole spectral range. The much lower *J*<sub>sc</sub> in solar cells with 42 °C step I temperature may also originate from the presence of photoinactive domains ( $\delta$ -phase) in the perovskite film, as will be discussed later. Solar cells prepared at 50 °C exhibit a higher V<sub>oc</sub> and *J*<sub>sc</sub> than solar cells made with 55 and 60 °C step I temperatures. Figure 4e shows the shelf-lifetime of solar cells prepared at the discussed temperatures. In this measurement, *J*–*V* curves on at least 12 cells were measured on separate days, whereas in between, solar cells were kept in the dark under nitrogen. Figure 4e displays that solar cells made at 42 °C underwent rapid performance degradation. Solar cells prepared at 55 and 60 °C also showed a clear trend of degradation in the first 2 weeks, with 50 °C retaining the most performance. Figure 4f displays the MPP tracked photovoltaic performance of solar cells. It shows that solar cells made at 50 °C exhibit the best stability, with a *T*<sub>S80</sub> lifetime of  $\approx$ 300 h, whereas solar cells made at 42, 55, and 60 °C result in *T*<sub>S80</sub> lifetimes of 75, 164, and 217 h, respectively.

To better understand the differences in crystal structure between CsPbI<sub>1.8</sub>Br<sub>1.2</sub> perovskite films prepared at the four

different step I temperatures, we used XRD combined with GIWAXS of films, measured under vacuum. Compared with XRD, GIWAXS can provide information on the texture of crystals and minimizes misinterpretation of peak intensities in XRD by collecting 2D scattering/structural information. Using synchrotron radiation under vacuum can also help to identify smaller crystal domains to understand phase impurities better. Figure S8, Supporting Information, shows the scheme of the GIWAXS measurements, and Figure S9, Supporting Information, presents the peak assignment for the texture analysis. Figure S10, Supporting Information, shows the XRD pattern for CsPbI<sub>1.8</sub>Br<sub>1.2</sub> perovskite samples prepared at each temperature.

To investigate further, Figure 5a,b shows 2D GIWAXS patterns for samples prepared at 50 and 60 °C, with the 42 and 55 °C patterns given in Figure S11, Supporting Information. The azimuthally integrated 1D patterns from 2D data are given in Figure S12a, Supporting Information. In the case of the sample prepared at 42 °C, additional low-intensity scattering rings at  $2\theta$  of  $\approx$ 9.9° and 13.2° are assigned to the  $\delta$ -phase of the perovskite film; these features are highlighted in Figure S12b, Supporting

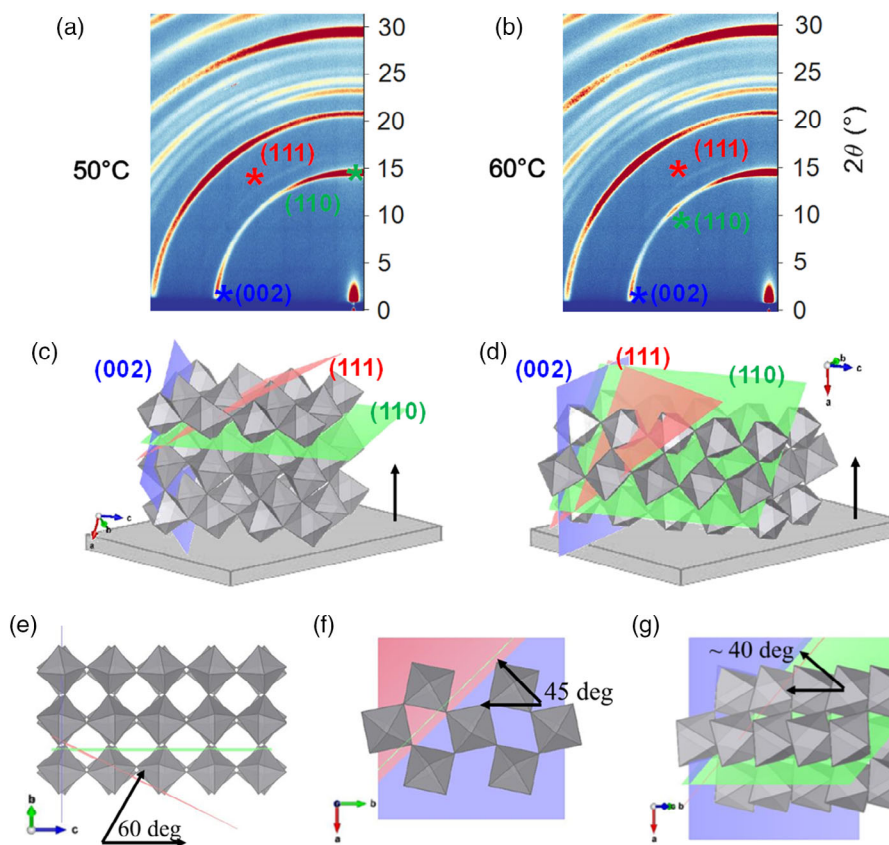


**Figure 5.** Understanding the influence of step I temperature on the final crystal structure of  $\text{CsPb}_{1.8}\text{Br}_{1.2}$  films. Representative 2D GIWAXS detector images for a)  $50^\circ\text{C}$  and b)  $60^\circ\text{C}$  in step I with grazing incidence angle of  $1^\circ$ . Schemes c,d) illustrate the two dominant texture orientations, relative to substrate, with lattice planes indicated. e–g) show different geometric slices with important angles arising in the image for samples prepared at c,e)  $50^\circ\text{C}$  and d,f,g)  $60^\circ\text{C}$ . Representative 2D GIWAXS detector images with incidence angles of  $2^\circ$  and  $3^\circ$  can be found in Figure S13, Supporting Information.

Information. The enlarged  $2\theta$  range in Figure S12c, Supporting Information, highlights a small peak shift of the scattering feature associated with the (004)/(220) planes, suggesting some variation in halide composition as the step I temperature is varied. This trend is most significant with the  $42^\circ\text{C}$  sample shifted to lower angles, indicating shrinking of the lattice with higher annealing temperatures, which could be explained by this step modifying the final film, such that more bromide becomes coordinated with Pb during this step.

Critically, we note that the (110)/(002) scattering ring for step I temperatures of  $42\text{--}55^\circ\text{C}$  is dominated by a single partial scattering ring in the OOP direction (Figure 5a,b and Figure S11, Supporting Information), with the orthogonal (002)/(110) scattering in-plane (IP). The (111) scattering ring has its maximum at  $60^\circ$ , expected for  $\langle 110 \rangle$  orientation, as shown in Figure 5c,e. However, this is not the case for the  $60^\circ\text{C}$  sample. Figure 5d,f,g shows that the (110) ring has a second intensity maximum at  $45^\circ$ , confirmed by the (111) ring also have higher intensity at  $\approx 40^\circ$ , corresponding to  $\langle 100 \rangle / \langle 020 \rangle$  orientation. The additional texture introduced in the  $60^\circ\text{C}$  sample is most likely caused by changes in biaxial strain during the initial crystallization process. Here, it is very interesting to see how the step I temperature could have such a significant influence on the final texture of perovskite films. As we discussed earlier in Figure 4, solar cells

with step I annealing temperature of  $60^\circ\text{C}$  are less photostable and suffer from a higher potential loss than devices fabricated at  $50^\circ\text{C}$  during step I. It indicates that the additional texture with (110) scattering at  $45^\circ$ , in addition to the OOP direction, may lead to worsened photostability observed in the MPP tracking measurements.

### 3. Conclusion

In summary, we found that the step I annealing temperature was critically important for management of phase purity and crystal orientation of inorganic perovskites and, thus, significantly influences the photovoltaic performance and operational stability of inorganic perovskite solar cells. The difference in textures of the final perovskite films is most likely caused by the changes in biaxial strain during the initial crystallization. Moreover, in the studied perovskites solar cells, the optimized annealing temperature decreases with an increase in bromide ratio in  $\text{CsPbI}_{3-x}\text{Br}_x$ . With a low step I temperature of  $50^\circ\text{C}$ ,  $\text{CsPb}_{1.8}\text{Br}_{1.2}$  exhibited a pure orthorhombic phase and only one crystal orientation of the (110) plane. Consequently, this allowed for the highest efficiency of up to 14.6%. Starting with an average efficiency of 12.9%,  $\text{CsPb}_{1.8}\text{Br}_{1.2}$  perovskite solar



cells achieved the  $T_{S80}$  lifetimes of  $\approx 300$  h, averaged of over six solar cells, following the ISOS-L-II protocol. In contrast, CsPbI<sub>2.0</sub>Br<sub>1.0</sub> and CsPbI<sub>2.2</sub>Br<sub>0.8</sub> solar cells, due to phase impurity in their perovskite films, presented an initial average efficiency of 11.9% and 10.8% and resulted in a  $T_{S80}$  of around 192 and 134 h. It should also be noted that solar cells composed of high I-rich compositions of CsPbI<sub>2.4</sub>Br<sub>0.6</sub> and CsPbI<sub>2.7</sub>Br<sub>0.3</sub> exhibited a poor photovoltaic performance and operational stability. Alternative strategies must continue to develop to enhance the phase purity and thermodynamic stability of more I-rich cesium lead halides.

## Supporting Information

Supporting Information is available from the Wiley Online Library or from the author.

## Acknowledgements

J.A.S. acknowledges the EPSRC Centre for Doctoral Training in New and Sustainable Photovoltaics (CDT-PV) for studentship funding. J.A.S. acknowledges financial support from the Research Foundation—Flanders (FWO Grant No. 12Y7218N). M.S. acknowledges the Deutsche Forschungsgemeinschaft (DFG, German Research Foundation, project number of 423749265). Q.W. appreciated the kind assistance from Mrs. Klimm Carola for the SEM measurements and Dr. Michael Tovar for his kind assistance with XRD measurements.

## Conflict of Interest

The authors declare no conflict of interest.

## Author Contributions

Q.W. designed the experiment, drafted the manuscript, fabricated, and characterized the solar cells and prepared the samples for the measurements involved in this work. J.A.S. and D.S. conducted and contributed to the data analysis of the GIWAXS measurements for this work. J.A.S. conducted refinement for the crystal structure and texture analysis of the studied inorganic perovskite thin films. C.M.W., P.C., and M.S. conducted and contributed to the data analysis of the PL measurements for this work. H.K. conducted the ageing test of solar cells in this study and contributed to the data analysis. M.L. and S.-H.T.-C. provided useful discussion during the conduction of the project. All authors discussed the results and provided feedback on the manuscript.

## Keywords

cesium lead halides, crystal orientation, inorganic perovskites, ISOS-L-II protocol, phase purity, photostability

Received: April 27, 2020

Revised: May 19, 2020

Published online:

- [1] a) F. J. Bai, J. Zhang, Y. F. Yuan, H. B. Liu, X. S. Li, C. C. Chueh, H. Yan, Z. L. Zhu, A. K. Y. Jen, *Adv. Mater.* **2019**, *31*, 1904735; b) M. Chen, M. G. Ju, H. F. Garces, A. D. Carl, L. K. Ono, Z. Hawash, Y. Zhang, T. Y. Shen, Y. B. Qi, R. L. Grimm, D. Pacifici, X. C. Zeng, Y. Y. Zhou, N. P. Padture, *Nat. Commun.* **2019**, *10*, 16; c) J. L. Duan, Y. Y. Zhao,

- Y. D. Wang, X. Y. Yang, Q. W. Tang, *Angew. Chem., Int. Ed.* **2019**, *58*, 16147; d) Q. D. Tai, K. C. Tang, F. Yan, *Energy Environ. Sci.* **2019**, *12*, 2375; e) W. C. Xiang, Z. W. Wang, D. J. Kubicki, X. T. Wang, W. Tress, J. S. Luo, J. H. Zhang, A. Hofstetter, L. J. Zhang, L. Emsley, M. Grätzel, A. Hagfeldt, *Nat. Commun.* **2019**, *10*, 4686.
- [2] Y. Wang, X. Liu, T. Zhang, X. Wang, M. Kan, J. Shi, Y. Zhao, *Angew. Chem., Int. Ed.* **2019**, *58*, 16691.
- [3] A. Al-Ashouri, A. Magomedov, M. Roß, M. Jošt, M. Talaikis, G. Chistiakova, T. Bertram, J. A. Márquez, E. Köhnen, E. Kasparavičius, S. Levenco, L. Gil-Escrig, C. J. Hages, R. Schlattmann, B. Rech, T. Malinauskas, T. Unold, C. A. Kaufmann, L. Korte, G. Niaura, V. Getautis, S. Albrecht, *Energy Environ. Sci.* **2019**, *12*, 3356.
- [4] a) Q. Wang, N. Phung, D. Di Girolamo, P. Vivo, A. Abate, *Energy Environ. Sci.* **2019**, *12*, 865; b) J. Xu, C. C. Boyd, Z. J. Yu, A. F. Palmstrom, D. J. Witter, B. W. Larson, R. M. France, J. Werner, S. P. Harvey, E. J. Wolf, W. Weigand, S. Manzoor, M. F. A. M. van Hest, J. J. Berry, J. M. Luther, Z. C. Holman, M. D. McGehee, *Science* **2020**, *367*, 1097.
- [5] a) J. A. Steele, H. Jin, I. Dovgaliuk, R. F. Berger, T. Braeckvelt, H. Yuan, C. Martin, E. Solano, K. Lejaeghere, S. M. J. Rogge, C. Notebaert, W. Vandezande, K. P. F. Janssen, B. Goderis, E. Debroye, Y.-K. Wang, Y. Dong, D. Ma, M. Saidaminov, H. Tan, Z. Lu, V. Dyadkin, D. Chernyshov, V. Van Speybroeck, E. H. Sargent, J. Hofkens, M. B. J. Roeflaers, *Science* **2019**, *365*, 679; b) R. J. Sutton, M. R. Filip, A. A. Haghighirad, N. Sakai, B. Wenger, F. Giustino, H. J. Snaith, *ACS Energy Lett.* **2018**, *3*, 1787; c) Q. Zhao, A. Hazarika, L. T. Schelhas, J. Liu, E. A. Gaulding, G. Li, M. Zhang, M. F. Toney, P. C. Sercel, J. M. Luther, *ACS Energy Lett.* **2020**, *5*, 238; d) T. Moot, A. R. Marshall, L. M. Wheeler, S. N. Habisreutinger, T. H. Schloemer, C. C. Boyd, D. R. Dikova, G. F. Pach, A. Hazarika, M. D. McGehee, H. J. Snaith, J. M. Luther, *Adv. Energy Mater.* **2020**, *10*, 1903365.
- [6] Y. Wang, M. I. Dar, L. K. Ono, T. Zhang, M. Kan, Y. Li, L. Zhang, X. Wang, Y. Yang, X. Gao, Y. Qi, M. Grätzel, Y. Zhao, *Science* **2019**, *365*, 591.
- [7] W. Ke, I. Spanopoulos, C. C. Stoumpos, M. G. Kanatzidis, *Nat. Commun.* **2018**, *9*, 4785.
- [8] H. Meng, Z. Shao, L. Wang, Z. Li, R. Liu, Y. Fan, G. Cui, S. Pang, *ACS Energy Lett.* **2020**, *5*, 263.
- [9] C. Liu, W. Z. Li, H. Y. Li, H. M. Wang, C. L. Zhang, Y. G. Yang, X. Y. Gao, Q. F. Xue, H. L. Yip, J. D. Fan, R. E. I. Schropp, Y. H. Mai, *Adv. Energy Mater.* **2019**, *9*, 1803572.
- [10] R. J. Sutton, G. E. Eperon, L. Miranda, E. S. Parrott, B. A. Kamino, J. B. Patel, M. T. Hörantner, M. B. Johnston, A. A. Haghighirad, D. T. Moore, H. J. Snaith, *Adv. Energy Mater.* **2016**, *6*, 1502458.
- [11] S. S. Mali, J. V. Patil, C. K. Hong, *Adv. Energy Mater.* **2020**, *10*, 1902708.
- [12] H. Zhao, Y. Han, Z. Xu, C. Y. Duan, S. M. Yang, S. H. Yuan, Z. Yang, Z. K. Liu, S. Z. Liu, *Adv. Energy Mater.* **2019**, *9*, 1902279.
- [13] S. Sanchez, N. Christoph, B. Grobety, N. Phung, U. Steiner, M. Saliba, A. Abate, *Adv. Energy Mater.* **2018**, *8*, 1802060.
- [14] E. Köhnen, M. Jošt, A. B. Morales-Vilches, P. Tockhorn, A. Al-Ashouri, B. Macco, L. Kegelmann, L. Korte, B. Rech, R. Schlattmann, B. Stannowski, S. Albrecht, *Sustainable Energy Fuels* **2019**, *3*, 1995.
- [15] a) A. Rajagopal, R. J. Stoddard, H. W. Hillhouse, A. K. Y. Jen, *J. Mater. Chem. A* **2019**, *7*, 16285; b) M. Lyu, M. Zhang, N. A. Cooling, Y. Jiao, Q. Wang, J.-H. Yun, B. Vaughan, G. Triani, P. Evans, X. Zhou, K. Feron, A. Du, P. Dastoor, L. Wang, *Sci. Bull.* **2016**, *61*, 1558.
- [16] R. Lin, K. Xiao, Z. Qin, Q. Han, C. Zhang, M. Wei, M. I. Saidaminov, Y. Gao, J. Xu, M. Xiao, A. Li, J. Zhu, E. H. Sargent, H. Tan, *Nat. Energy* **2019**, *4*, 864.
- [17] D. Zhao, C. Chen, C. Wang, M. M. Junda, Z. Song, C. R. Grice, Y. Yu, C. Li, B. Subedi, N. J. Podraza, X. Zhao, G. Fang, R.-G. Xiong, K. Zhu, Y. Yan, *Nat. Energy* **2018**, *3*, 1093.

- [18] A. F. Palmstrom, G. E. Eperon, T. Leijtens, R. Prasanna, S. N. Habisreutinger, W. Nemeth, E. A. Gaubing, S. P. Dunfield, M. Reese, S. Nanayakkara, T. Moot, J. Werner, J. Liu, B. To, S. T. Christensen, M. D. McGehee, M. F. A. M. van Hest, J. M. Luther, J. J. Berry, D. T. Moore, *Joule* **2019**, *3*, 2193.
- [19] W. Chen, H. Chen, G. Xu, R. Xue, S. Wang, Y. Li, Y. Li, *Joule* **2019**, *3*, 191.
- [20] a) S. De Wolf, J. Holovsky, S.-J. Moon, P. Löper, B. Niesen, M. Ledinsky, F.-J. Haug, J.-H. Yum, C. Ballif, *J. Phys. Chem. Lett.* **2014**, *5*, 1035; b) Q. Wang, C. Jiang, P. Zhang, T. W. Hamann, *J. Phys. Chem. C* **2018**, *122*, 14177.
- [21] a) Y. Guo, O. Yaffe, T. D. Hull, J. S. Owen, D. R. Reichman, L. E. Brus, *Nat Commun* **2019**, *10*, 1175; b) Y. Kanemitsu, *J. Mater. Chem. C* **2017**, *5*, 3427.
- [22] M. C. Brennan, J. Zinna, M. Kuno, *ACS Energy Lett.* **2017**, *2*, 1487.
- [23] a) P. Cottingham, R. L. Brutchey, *Chem. Commun.* **2016**, *52*, 5246; b) J. B. Hoffman, G. Zaiats, I. Wappes, P. V. Kamat, *Chem. Mater.* **2017**, *29*, 9767.
- [24] a) J. Wang, J. Zhang, Y. Zhou, H. Liu, Q. Xue, X. Li, C.-C. Chueh, H.-L. Yip, Z. Zhu, A. K. Y. Jen, *Nat. Commun.* **2020**, *11*, 177; b) D. Bai, H. Bian, Z. Jin, H. Wang, L. Meng, Q. Wang, S. Liu, *Nano Energy* **2018**, *52*, 408.
- [25] D. Kiermasch, L. Gil-Escrig, H. J. Bolink, K. Tvingstedt, *Joule* **2019**, *3*, 16.
- [26] M. V. Khenkin, E. A. Katz, A. Abate, G. Bardizza, J. J. Berry, C. Brabec, F. Brunetti, V. Bulović, Q. Burlingame, A. Di Carlo, R. Cheacharoen, Y.-B. Cheng, A. Colsmann, S. Cros, K. Domanski, M. Dusza, C. J. Fell, S. R. Forrest, Y. Galagan, D. Di Girolamo, M. Grätzel, A. Hagfeldt, E. von Hauff, H. Hoppe, J. Kettle, H. Köbler, M. S. Leite, S. Liu, Y.-L. Loo, J. M. Luther, C.-Q. Ma, et al., *Nat. Energy* **2020**, *5*, 35.
- [27] B. Wang, N. Novendra, A. Navrotsky, *J. Am. Chem. Soc.* **2019**, *141*, 14501.
- [28] a) M. Stolterfoht, C. M. Wolff, J. A. Márquez, S. Zhang, C. J. Hages, D. Rothhardt, S. Albrecht, P. L. Burn, P. Meredith, T. Unold, D. Neher, *Nat. Energy* **2018**, *3*, 847; b) C. M. Wolff, P. Caprioglio, M. Stolterfoht, D. Neher, *Adv. Mater.* **2019**, *31*, 1902762; c) P. Caprioglio, M. Stolterfoht, C. M. Wolff, T. Unold, B. Rech, S. Albrecht, D. Neher, *Adv. Energy Mater.* **2019**, *9*, 1901631.
- [29] M. Stolterfoht, P. Caprioglio, C. M. Wolff, J. A. Márquez, J. Nordmann, S. Zhang, D. Rothhardt, U. Hörmann, Y. Amir, A. Redinger, L. Kegelman, F. Zu, S. Albrecht, N. Koch, T. Kirchartz, M. Saliba, T. Unold, D. Neher, *Energy Environ. Sci.* **2019**, *12*, 2778.
- [30] Q. Wang, E. Mosconi, C. Wolff, J. Li, D. Neher, F. De Angelis, G. P. Suranna, R. Grisorio, A. Abate, *Adv. Energy Mater.* **2019**, *9*, 1900990.